G53D-0931

Results of InSAR and GPS Measurement of Tectonic Deformation of the Eastern California Shear Zone and Yucca Mountain, Nevada

W.C. Hammond[1], Zhenhong Li[2], Hans-Peter Plag[1], Geoff Blewitt[1], Corne Kreemer[1]

1) Nevada Geodetic Laboratory, Nevad Bureau of Mines and Geology, University of Nevada, Reno

2) Department of Geomatic Engineering, University College London, London, WC1E 6BT, United Kingdom

whammond@unr.edu

Introduction

Crustal deformation between the Sierra Nevada microplate and the central Basin and Range in Nevada is characterized by dextral shear and extension, exhibiting a velocity gradient 10-12 mm/yr [*Thatcher et al.*, 1999]. Approximately 1 mm/yr of this occurs across a zone ~100 km wide centered near Yucca Mountain, NV [*Wernicke et al.,* 2004; *Hill and Blewitt*, 2006]. Quantification and characterization of this deformation is important for studies of Basin and Range tectonics, western U.S continental dynamics, and for evaluation of potential seismic risks to the high level nuclear waste repository at Yucca Mountain, NV.

Here we build on the work of *Peltzer et al.*, 2001, *Wright et al.*, 2004, and *Katzenstein and Bell*, [2005], who have explored the ability of Interferometric Synthetic Aperture Radar (InSAR) to provide constraints on secular strain accumulation on active faults. Our study area includes a portion of the Eastern California Shear Zone (ECSZ) that was previously studied by *Peltzer et al.*, 2001, but we focus on track 399 which lies just east of, and overlaps, their study area. Additionally, we include frame 2871, north of frame 2889, that includes the Yucca Mountain region, the Death Valley, Panamint Valley area, the eastern termination of the Garlock Fault, and the northernmost Mohave Desert.

Because of the dense Global Positioning System (GPS) and InSAR coverage, our study area offers an excellent opportunity to measure the value of combining InSAR and GPS in crustal deformation studies. In our approach, we improve our ability to infer the spatial pattern of surface deformation by combining data from the BARGEN continuous GPS cluster that is deployed near Yucca Mountain, NV and ERS1 and ERS2 missions. We solve for an integrated surface deformation model that honors both sets of constraints (see box below for explanation of technique). Additionally we calibrate the interferograms using 1) a model of horizontal tectonic deformation obtained from GPS [*Kreemer et al.*, 2006] and 2) the zenith path delays associated with tropospheric water vapor using the GTTM method of *Li et al.*, [2006].

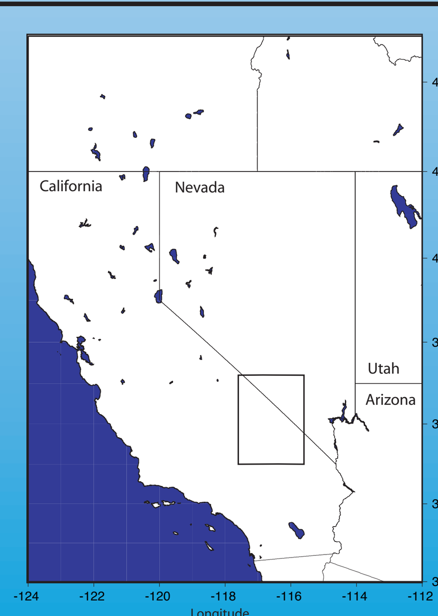

Right) Location of radar scenes for track 399 frame 2871 and 2889 (black outlines) and continous GPS sites of the southern BARGEN network (red triangles). Holocene and Quaternary faults are shown with gray line segments. Above) Location of our study area in the westernmost Basin and Range of southern Nevada, and eastern California .

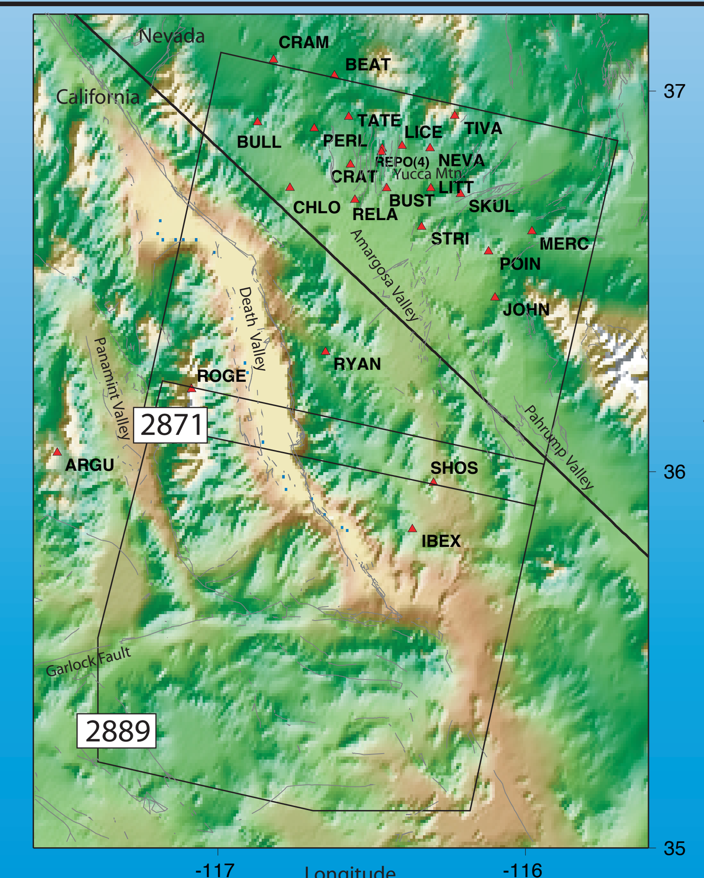

Method

The interseismic signal associated with tectonic deformation in our study area is small, ~1 mm/yr of horizontal deformation near Yucca Mountain projects to ~0.3 mm/yr in the radar line of site, and about a factor of 10 larger across the entire ECSZ. Noise sources include 1) spatial variability of tropospheric water vapor delays, 2) phase ramps associated with orbit errors and/or long wavelength gradients in the atmosphere, 3) surface motions not associated with permanent tectonic deformation.

We reduce the impact of these unwanted signals through a combination of calibration and stacking. The analytical steps are illustrated in the figures to the right. We begin by selecting ERS radar pairs with short perpendicular baselines, and long temporal separation (as long as ~9 years, see baseline figures right). Prior to stacking we adjust each interferogram to:

1) Adjust for the tropospheric water vapor delays using the topography-dependent atomspheric turbulence model correction (GTTM) of *Li et al.*, [2006]. This technique interpolates the GPS zenith delay estimates and digital elevation model (DEM) to create an estimated water vapor delay map. This map is subtracted from the interferogram. Our study area has high topographic relief and thus these effects can be on the order of several cm of apparent motion inside the scene.

2) Remove quadratic phase ramps associated with non-tectonic signals (e.g. orbit errors, etc.)

3) Explicity preseve the effects of interseismic tectonic deformation by subtracting before phase ramp adjustent the strain map velocities of *Kreemer et al.*, [2006], which is a spatial interpolation of GPS velocities.

The example shown here is for a single frame 2871 interferogram with short temporal separation. For the stacking we applied these steps to each of four pairs with long temporal separation for frames 2871 and 2889.

Note that the integration of GPS with InSAR occurs at two levels, 1) for calibration of the wator vapor and 2) for removal of phase ramps not associated with horizontal tectonic deformation.

Combining GPS and InSAR to Obtain Surface Deformation Models that are Consistent with Both Datasets

Objective: obtain a stacked interferogram that has been corrected for phase ramps that are associated with orbital errors but has not removed the effects of long wavelength horizontal tectonics that are known to occur in the western Great Basin, and that have a large enough signal to be detected in the interferogram.

Solution: Subtract the predicted effects of horizontal tectonics from the interferogram before calculating the quadratic error surface $Q(\lambda,\phi) = A\lambda^2 + B\phi^2 + C\lambda\phi + D\lambda + E\phi + F$ as a function of latitude λ and longitude ϕ. We assume that the unwrapped interferogram $\Phi(\lambda,\phi)$ is the sum of 1) the desired true surface deformation signal $\vec{S}(\lambda,\phi)$, 2) the long wavelength error term and 3) the effects of water vapor in the atmosphere $Z(\lambda,\phi)$ which are estimated from GPS zenith path delays using the method of *Li et al.*, 2006

$$\Phi(\lambda,\phi) = Q(\lambda,\phi) + Z(\lambda,\phi) + \vec{S}(\lambda,\phi)\cdot\vec{v}_S \qquad (1)$$

where $\vec{v}_S$ is the vector pointing from the ground to the satellite.

The surface deformation vector is partially constrained by the horizontal deformation field, which is obtained from GPS, and estimated by the strain map $\vec{C}(\lambda,\phi)$ which is a vector field having zero for all vertical motion. Expressing the strain map in terms of the surface motion

$$\vec{C}(\lambda,\phi) \approx \vec{S}(\lambda,\phi) - [\vec{S}(\lambda,\phi)\cdot\vec{u}_z]\vec{u}_z \qquad (2)$$

where $\vec{u}_z$ is the unit vertical vector. We assume that horizontal deformation that is spatially coherent over long wavelengths dominates over any vertical signal of the same wavelength. Thus the angle between the vertical and $\vec{S}(\lambda,\phi)$ is usually close to 90°. This is true for long wavelength signal that we wish to preserve, and thus subtract from $\Phi(\lambda,\phi)$ before using it to estimate $Q(\lambda,\phi)$. Thus the second term in (2) will be close to zero and for the purpose of forming the correction we can approximate

$$\vec{C}(\lambda,\phi) \approx \vec{S}(\lambda,\phi) \qquad (3)$$

so we solve for A through F in $Q(\lambda,\phi) = A\lambda^2 + B\phi^2 + C\lambda\phi + D\lambda + E\phi + F$ where

$$Q(\lambda,\phi) = \Phi(\lambda,\phi) - \vec{C}(\lambda,\phi)\cdot\vec{v}_S - Z(\lambda,\phi) \qquad (4)$$

Thus, we use the strain map (from GPS) to find the correction for each interferogram pair. Then stack the corrected pairs and estimate surface deformation rate using

$$\vec{S}(\lambda,\phi)\cdot\vec{v}_s = \frac{\sum \Phi_i(\lambda,\phi) - Q_i(\lambda,\phi) - Z(\lambda,\phi)}{T(\lambda,\phi)} \qquad (5)$$

where the division on the right-hand side is point-wise division by the total summed intervals in the stack $T(\lambda,\phi)$ at each point.

Example ERS interferogram Frame 2871 000327-000918 (Made Using ROI_PAC) Black Triangles are BARGEN Continuous GPS sites

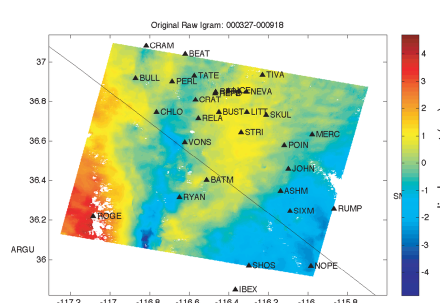

CALIBRATIONS

Horitonal GPS Interpolated Strain Rate/Velocity Map

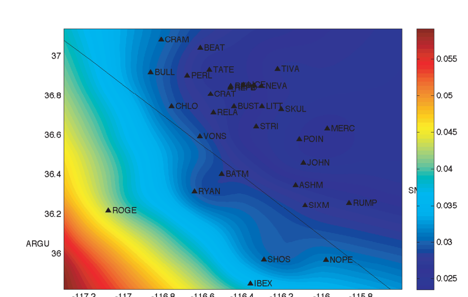

Water Vapor+Topography Interpolation

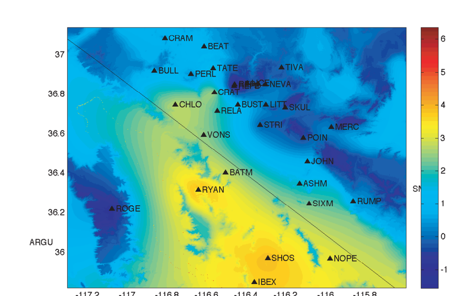

Remaining Phase Ramp Orbit Error + ???

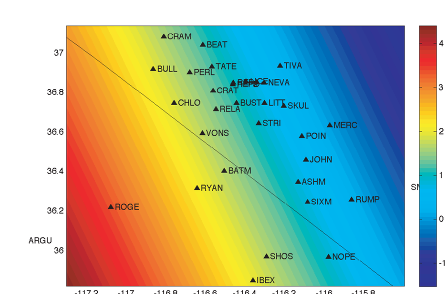

Corrected for Strain Map and GTTM Water Vapor

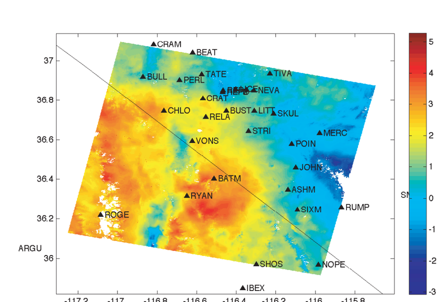

Corrected for Strain Map GTTM Vapor, and Ramp

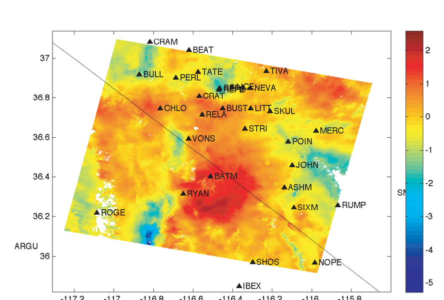

+ Smoothing

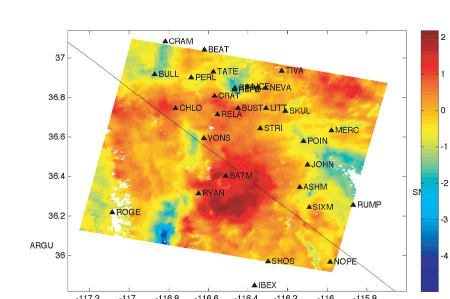

Right) Because we wish to identify the signal associated with permanent displacements associated with tectonic deformation, we exclude areas with the softest rocks in the valley bottoms. A geologic map [*Workman et al.*, 2002] was used to create a screen defined by the youngest Quaternary and Holocene surfaces. These areas are more susceptabile to rapid and sometimes seasonal vertical movements associated with hydrologic processes [e.g. see *Burgmann et al.,* 2006] and generally do not reflect secular tectonics.

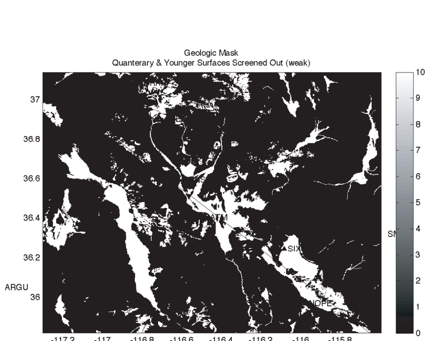

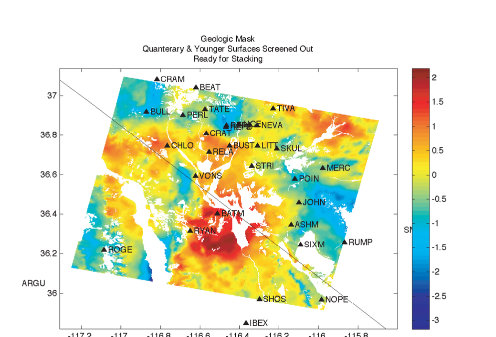

STACK of 4 ERS Pairs/Frame

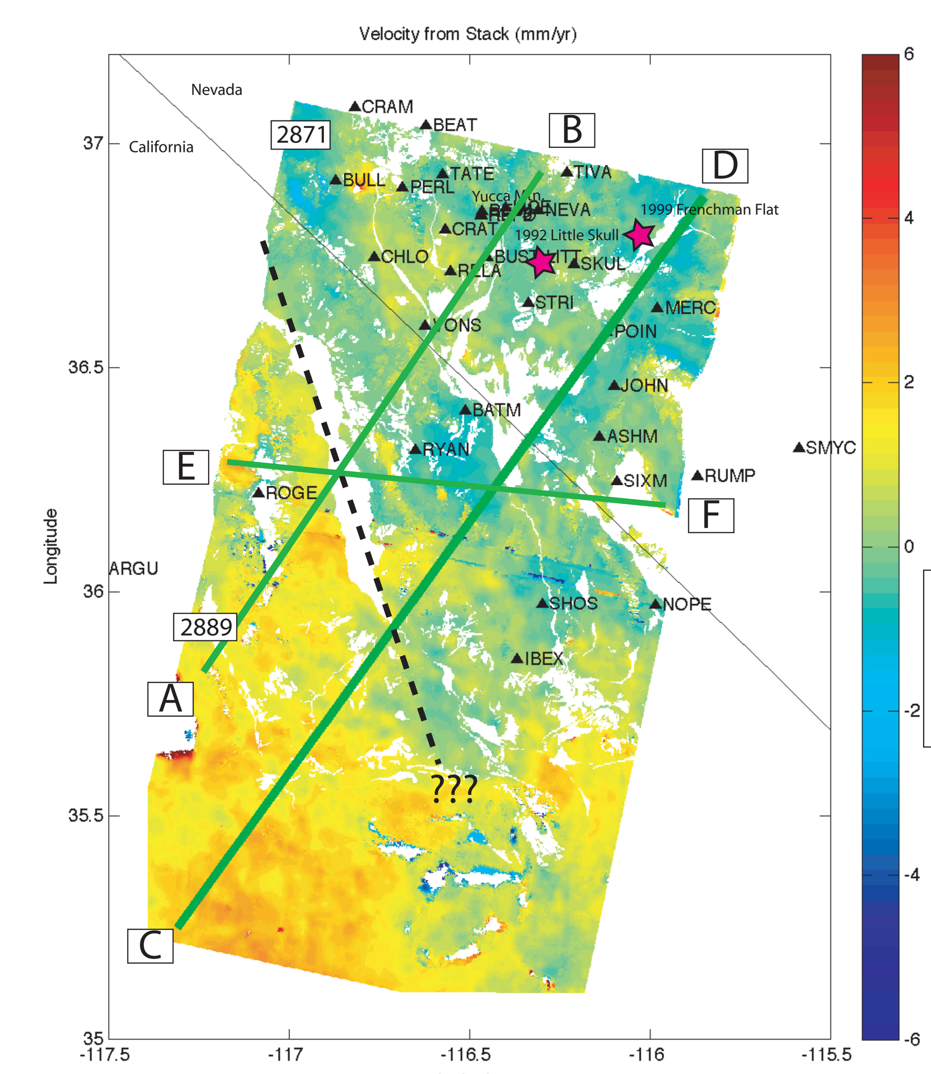

Line of Sight Velocity (mm/yr)

Left) Stack of calibrated interferograms.

The transition between slowly and rapidly moving crust appears abrupt across Death Valley (highlighted by black dashed line). The trend in the radar-derived velocity image terminates near the eastern end of the Garlock Fault, and the continuation of this velocity contrast to the south is less clear. It is possible, however, that this change in displacement rate maps the eastern boundary of the most rapidly deforming part of the ECSZ.

The stack reveals subsidence associated with the Bullfrog mine ground water withdrawal near the town of Beatty, NV (near the GPS site BULL). However, our applied geologic mask hides subsidence that was observed by *Katzenstein and Bell,* 2005, in the Pahrump valley (between GPS sites SIXM, RUMP and NOPE), and also subsidence assocated with the 1999 Frenchman Flat and 1992 Little Skull earthquakes.

The InSAR Signal vs. the GPS signal

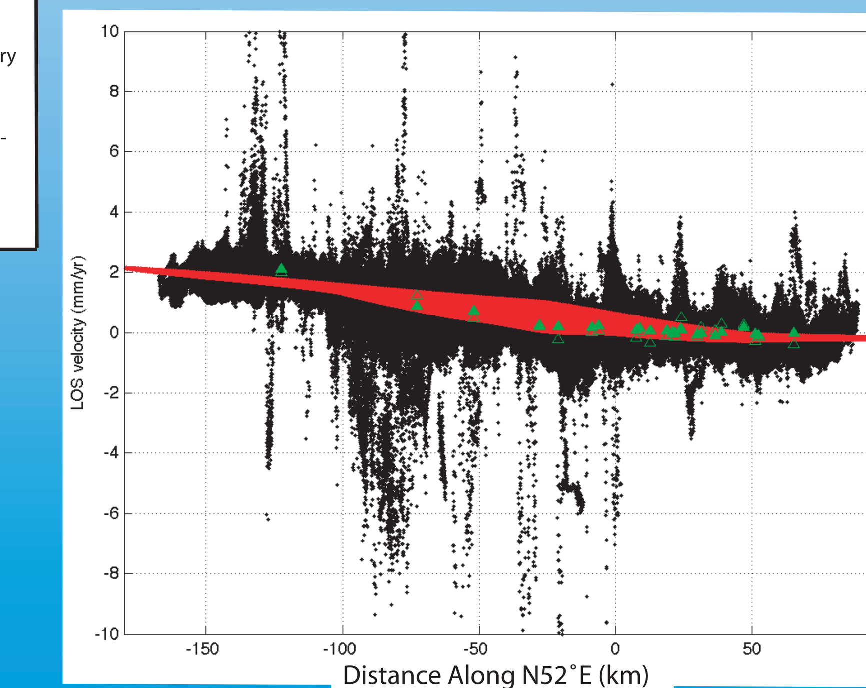

Right) Stacked interferogram velocity scattergram (black dots) is shown under the strain map velocities projected into the satellite line of sight (red). Every pixel shown in the stack (far left) is also shown in the scattergram. Isolated subsidence/uplift features are visible as deviations from main trend in stack. (Note that subsidence in this figure plots above the trend since its increasing line of sight).

The GPS velocities of the BARGEN network (horizontal only) projected to line of sight are shows with green solid triangles. The BARGEN three component GPS velocities projected into line of sight are shown with green open triangles. The width of the red band is the result of strain map velocities varying normal to the plane of this projection, which is normal to the trend of the average shear transport direction in the ECSZ.

The comparison between these different representations of the deformation field shows that the scatter in the InSAR measurements (RMS=2.7 mm/yr) is much greater than the GPS. The scatter will be reduced in the future, when more interferometric pairs are brought into the stack, and when our methods for calibrating out the atmosphere improve.

Stacked Interferogram Velocity vs. Strain Map

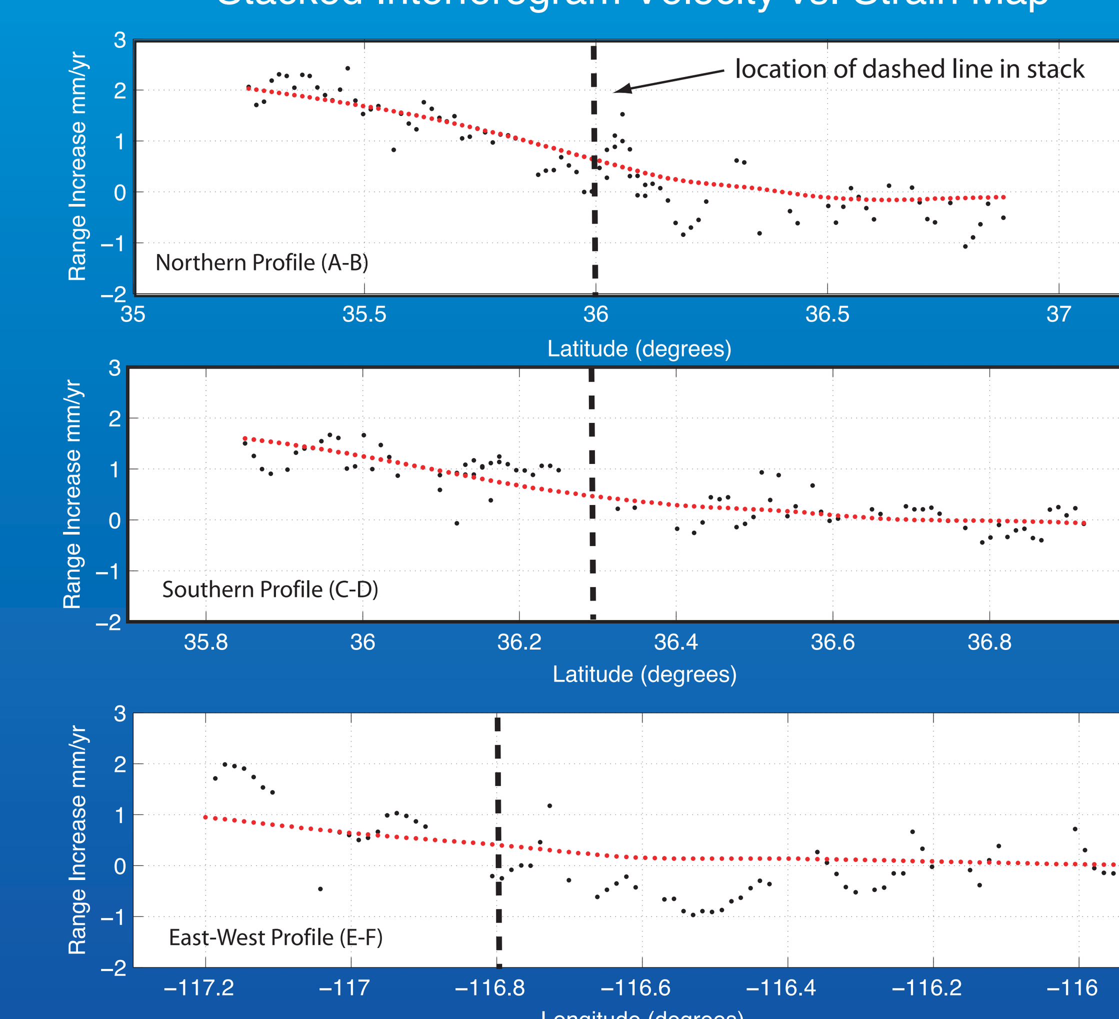

Left) There appears to be an abrupt change in the displacement rate where the profiles (green line spanning stack image far left) cross the black dotted line, in the vicinity of Death Valley. This change coincides with a transition from predominantly cool colors to the east to predominantly warm colors to the west in the stack figure. (Note that positive range increase coincides with greater northwest trending motion or subsidence).

Given our methodology of removing phase ramps not consistent with GPS-measured crustal deformation, the long-wavelength trend across the stack is constrained by the interpolated GPS compilation strain map of *Kreemer et al.* [2006] (red dots left). Note that the compilation includes data from other networks (near and far field) as well as BARGEN.

The signal associated with shorter wavelength features should be present in the InSAR results across the transect (black dots). It is at present partially obscured by the noise sources discussed in the lower left corner of this poster. However, intermediate wavelength features are also present (e.g. changes in rate across Death Valley) and may reveal greater detail in the crustal deformation field, as is suggested by the boundary indicated by the dashed line.

Below) Baseline figures showng the ERS1/2 data that has been so far considered. Red lines indicate the pairs of radar scenes that were incorporated into the stack shown above left. Vertical red bars show the time of occurrence of notable earthquakes between 1992 and 2006. The Landers and Hector Mine events occured south of our study area. Location of the 1999 Frencham Flat and 1992 Little Skull Mountain earthquakes are shown on the stack figure (above) with magenta stars.

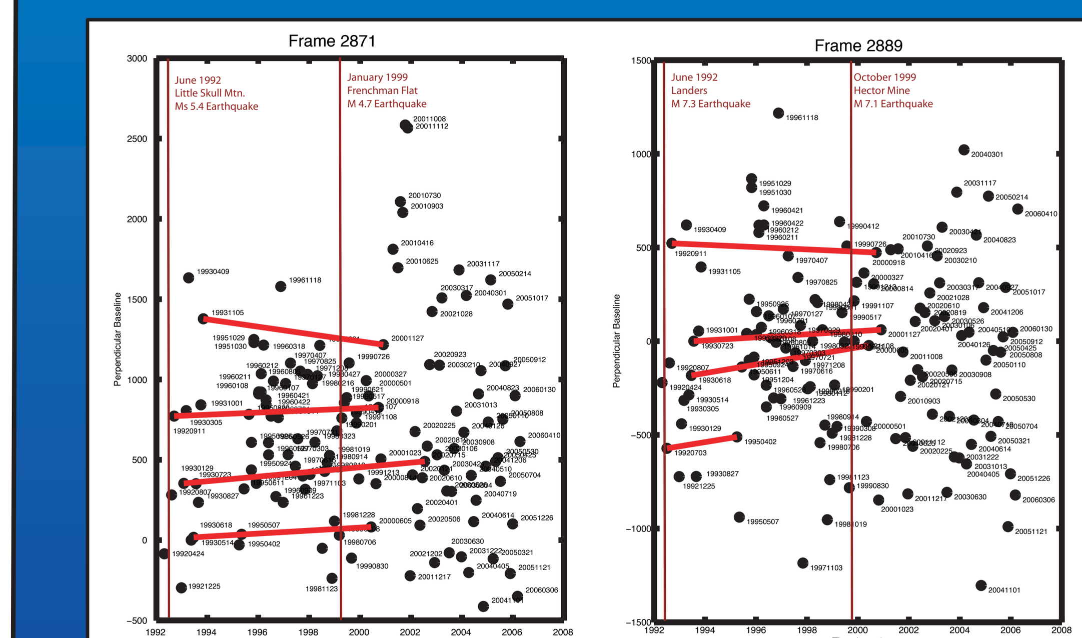

Other New Developments: Skye Sonora Landis Hammond born: 11/2/06

Improving Constraints on Crustal Deformation:

A measure of the added benefit that the InSAR results bear on permanent crustal deformation is whether the map of line of sight velocity (stack above) can improve estimates of slip rates on faults using a block modeling approach.

Block modeling (with schematic possible boundaries shown to the right) assumes that the crust is broken into discrete blocks bounded by faults that are locked at the surface but slip at depth at a rate equal to their long term slip rate. This type of analysis is especially useful when the number of crustal blocks is expected to be small, when geologic studies have provided data on the geometry of fault traces, and when we have constraints on the slip rates, style of faulting, and/or subsurface geometry of the faults. Furthermore, the block modeling "filter" will tend to de-ephasized noise that has a short spatial wavelength, such as that originating from atmospheric effects, as long as the block dimensions are generally larger than the atmospheric disturbances.

The InSAR data is sensitive to gradients in velocity with a resolution much smaller that the dimensions of the crustal blocks in our study area. Thus constraint on vertical axis rotations of blocks, and along-strike variations in slip rates may be improved by including InSAR results in the constraint.

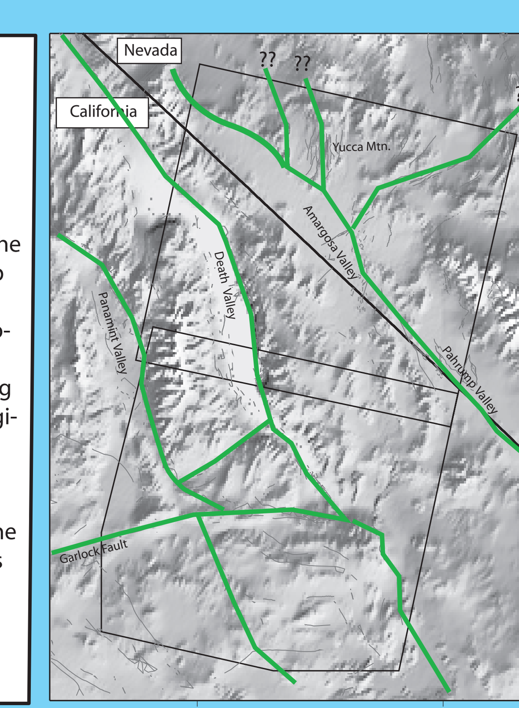

Future Enhancements Coming Soon:

- Process recently obtained additional ERS scenes, including ascending tracks, and add to the stack to further reduce noise in the line of sight velocity.
- Include Envisat scenes
- Process two frames 2871 and 2889 together in roi_pac to reduce effects of discontinuity near the frame boundary.
- Include SCIGN GPS sites in Mohave Desert and ECSZ to provide greater detail to GPS strain map and improve resolution of GTTM water vapor calibration in the southern part of frame 2889.
- Use Zhenhong Li's time-series approach to stacking.
- Use LOS velocity map plus GPS to constrain fault slip rates.

References

Burgmann, R., G. Hilley, A. Ferretti, and F. Novali, 2006, Resolving vertical tectonics in the San Francisco Bay Area from permanent scatterer InSAR and GPS analysis, Geology, 34 (3), 221-224.

Hill, E., and G. Blewitt (2006), Testing for fault activity at Yucca Mountain, Nevada, using independent GPS results from the BARGEN network, Geophys. Res. Lett., 33, L14302, doi:10.1029/2006GL026140.

Katzenstein, K. W., and J. W. Bell (2005), InSAR Reveals a Potpourri of Deformation Signals in the Yucca Mountain -- Amargosa Valley -- Death Valley Region, Southwestern Nevada/Southeastern California, Eos Trans. AGU, 86(52), Fall Meeting Abstract G51C-0844.

Kreemer, C., G. Blewitt, and W. C. Hammond (2006), Geodetic constraints on contemporary deformation in the northern Walker Lane: 2, velocity and tensor strain rate analysis, Late Cenozoic Structure and Evolution of the Great Basin – Sierra Nevada Transition.

Li, Z., E. J. Fielding, P. Cross, and J.-P. Muller (2006), Interferometric synthetic aperture radar atmospheric correction: GPS topography-dependent turbulence model, J. Geophys. Res., 111, B02404, doi:10.1029/2005JB003711.

McCaffrey, R. (2005), Block kinematics of the Pacific-North America plate boundary in the southwestern United States from inversion of GPS, seismological and geologic data, J. Geophys. Res., 110, B7, doi:10.1029/2004JB002207.

Peltzer, G., F. Crampe, S. Hensley, and P. Rosen (2001), Transient strain accumulation and fault interaction in the Eastern California shear zone, Geology, 29(11), 975-978.

Thatcher, W., G. R. Foulger, B. R. Julian, J. L. Svarc, E. Quilty, and G. W. Bawden (1999), Present-day deformation across the Basin and Range province, western United States, Science, 283, 1714-1718.

Wernicke, B. P., J. L. Davis, R. A. Bennett, J. E. Normandeau, A. M. Friedrich, and N. A. Niemi (2004), Tectonic Implications of a dense continuous GPS velocity field at Yucca Mountain, Nevada, J. Geophys. Res., 109, B12404.

Workman, J.B., C.M. Menges,W.R.Page, E.M. Taylor, E.G. Ekren, P.D. Rowley, G.L. Dixon, R.A. Thompson, L.A.Wright, (2002), Geologic Map o fthe Death Valley Ground-Water Model Area, Nevada and California.

Wright, T. J., B. Parsons, P. C. England, and E. J. Fielding (2004), InSAR observations of Low slip rates on the Major faults of western Tibet, Science, 305(236-239.

Acknowledgements:

This research has been support by a grant from the Department of Energy Yucca Mountain project Task 3 "Geodetic Monitoring of the Yucca Mountain Region using Continuous Global Positioning System Measurements". This project has made use of the "Repeat Orbit Interferometry Package (ROI_PAC) made available by the Jet Propulsion Laboratory via the Open Channel Software Foundation.